

Tracing Quasar Narrow-Line Regions Across Redshift: A Library of High S/N Optical Spectra

A. Tammour^{*1}, S. C. Gallagher¹, & Gordon Richards²

¹ *University of Western Ontario*

² *Drexel University*

27 May 2022

ABSTRACT

In a single optical spectrum, the quasar narrow-line region (NLR) reveals low density, photoionized gas in the host galaxy interstellar medium, while the immediate vicinity of the central engine generates the accretion disk continuum and broad emission lines. To isolate these two components, we construct a library of high S/N optical composite spectra created from the Sloan Digital Sky Survey (SDSS-DR7). We divide the sample into bins of continuum luminosity and $H\beta$ FWHM that are used to construct median composites at different redshift steps up to 0.75. We measure the luminosities of the narrow-emission lines $[\text{Ne V}]\lambda 3427$, $[\text{Ne III}]\lambda 3870$, $[\text{O III}]\lambda 5007$, and $[\text{O II}]\lambda 3728$ with ionization potentials (IPs) of 97, 40, 35, and 13.6 eV respectively. The high IP lines' luminosities show no evidence of increase with redshift consistent with no evolution in the AGN SED or the host galaxy ISM illuminated by the continuum. In contrast, we find that the $[\text{O II}]$ line becomes stronger at higher redshifts, and we interpret this as a consequence of enhanced star formation contributing to the $[\text{O II}]$ emission in host galaxies at higher redshifts. The SFRs estimated from the $[\text{O II}]$ luminosities show a flatter increase with z than non-AGN galaxies given our assumed AGN contribution to the $[\text{O II}]$ luminosity. Finally, we confirm an inverse correlation between the strength of the $\text{Fe II}\lambda 4570$ complex and both the $[\text{O III}]$ EW (though not the luminosity) and the width of the $H\beta$ line as known from the eigenvector 1 correlations.

Key words: catalogues – (galaxies:) quasars: emission lines.

1 INTRODUCTION

The current paradigm of active galactic nuclei (AGN) includes a central source that comprises a super-massive black hole (SMBH) surrounded by an accretion disk (Antonucci 1993; Urry & Padovani 1995). Through this accretion disk, material gets funnelled into the SMBH (Shakura & Sunyaev 1973). Quasars are the most luminous class of AGN with bolometric luminosities of up to 10^{48} erg s^{-1} .

Photoionization by radiation from the accretion disk is thought to be the main mechanism through which gas in AGNs is ionized (Osterbrock & Ferland 2006). Studying the interactions between the ionizing photons and the material they encounter allows us to study the physical conditions in the ionized regions. For example, the presence of narrow forbidden lines in quasar spectra points to a region that has low density and is located relatively far from the black hole's sphere of influence. For the most part, the gas in the NLR region responds kinematically to the gravitational potential of the galaxy as a whole and therefore produces narrower

emission lines ($\text{FWHM} \leq 1000$ km s^{-1}) – hence its label. On the other hand, in the close vicinity of the central source (≤ 1 pc), the gas mainly feels the gravitational influence of the SMBH and therefore produces emission lines that are primarily Doppler-broadened with widths of 1000s km/s. We therefore call this region the broad-line region (BLR).

Though the broad and narrow-line regions are physically distinct, correlations between properties of the two regions are found in the literature. Most well-known are the so-called eigenvector 1 relations, first identified by Boroson & Green (1992, hereafter BG92) from principal component analysis of several spectral measurements of the low-redshift PG quasar sample. BG92 found that narrow $H\beta$ width, strong Fe II emission, and weak $[\text{O III}]$ emission tended to be found in the same objects. The strong eigenvector 1 objects have also been identified as having relatively high L/L_{Edd} values (e.g., Boroson & Green 1992; Boroson 2002; Sulentic et al. 2007). Given our understanding of the rather different origins of BLR and NLR emission, the linking of broad- and narrow-line spectral properties is puzzling, and the extended discussion in BG92 reflects this conceptual difficulty.

To first order, the NLR can be described as the dif-

* atammour@uwo.ca

fuse interstellar medium of the host galaxy illuminated by the accretion disk continuum. Quasar NLRs are therefore the regions where we expect the interactions between AGNs and their host galaxies to take place; the narrow emission lines are among the few tracers of the host galaxy that are evident in optical quasar spectra. It is therefore important to check that any apparent links between broad and narrow-line region spectral properties do not arise from secondary and unintentional selection effects of host galaxies. For example, the strong eigenvector 1 objects are necessarily low redshift (because of the lines used in the study), and therefore low luminosity. The original BG92 sample were all PG quasars, which because of their selection are not representative of the quasar population as a whole (Jester et al. 2005).

Therefore, we are interested in studying samples of quasars with very similar central engines across a range of redshift to determine if we can isolate the effects of host galaxy evolution on NLR emission. With the large Quasar Properties Catalogue of Shen et al. (2011) with 105,783 objects, this hypothesis can be tested by selecting similar types of quasars (in terms of L_{opt} and M_{BH}), and examining their narrow-line region properties independently.

Throughout this work we use: $\Omega_{\Lambda} = 0.7$, $\Omega_0 = 0.3$, $h = 0.7$ (Spergel et al. 2003).

2 DATA AND ANALYSIS

2.1 The Sample

The initial sample is selected from the Shen et al. (2011) catalogue of quasar properties (SDSS-DR7; Schneider et al. 2010; Shen et al. 2011). We restrict the sample to radio-quiet quasars (defined in the catalogue as objects with $R = f_{6\text{cm}}/f_{2500} < 10$; where $f_{6\text{cm}}$ and f_{2500} are the radio and optical flux densities observed at 6 cm and 2500 Å respectively). We also impose a redshift limit of $z \leq 0.75$ to ensure $\lambda_{\text{rest}} = 5100 \text{ \AA}$ is in our spectral range. This emission-line-free segment of the continuum is used to first normalize the spectra and later to calculate the relative line luminosities of the composites. The final sample contains 16,027 spectra. We utilize the OH-subtracted spectra of Wild & Hewett (2010) who constructed a set of the telluric-line-cleaned spectra (specifically around H β). We then apply IRAF’s DEREDDEN tool¹ to correct the spectra for Galactic extinction using the $E(B - V)$ values provided in the catalogue (Shen et al. 2011, and references therein). Finally, the spectra are shifted to the rest frame using the Hewett & Wild (2010) redshift determination as provided in Shen et al. (2011).

2.2 The Composites

One of the advantages of starting from a large homogeneous dataset like the SDSS quasar sample is the ability to stack objects to create higher signal-to-noise spectra which then allows us to examine weaker features (such as the high IP

[Ne v] line) that are otherwise hard to measure (e.g., Vanden Berk et al. 2001; Sulentic et al. 2002; Croom et al. 2002; Hill et al. 2014). To make sure we are identifying objects with similar AGN properties, we group objects according to their continuum luminosities at 5100 Å (L_{5100}) and the FWHM of H β ² as reported in Shen et al. (2011). These two quantities are often used in combination in the literature to estimate more physical properties of the AGN such as the mass of the SMBH and the accretion rate (Shen et al. 2011, and references therein, see also §2.3). We used the measured properties (luminosity and Balmer-line broad-line width) rather than derived properties (M_{BH} and L/L_{Edd}) to keep the binning process closer to the data. As shown later, in practice, our choice of binning also means that objects with similar values of M_{BH} and L/L_{Edd} are grouped together. One caveat is that the conversion of H β FWHM and L_{5100} into BH masses and L/L_{Edd} can be influenced by several factors such as the dependence of FWHM on our inclination angle to the broad-line region and the choice of bolometric correction for L_{5100} (e.g., Richards et al. 2006b). We start by sorting the objects according to their L_{5100} values and then dividing them into 10 groups with an equal number of objects (1602 or 1603). We choose to look at four of these groups with the low ($L1$: $\log L_{5100} = 43.15 - 44.17 \text{ erg s}^{-1}$), intermediate ($L4$: $\log L_{5100} = 44.36 - 44.45 \text{ erg s}^{-1}$ and $L7$: $\log L_{5100} = 44.63 - 44.72 \text{ erg s}^{-1}$), and high ($L10$: $\log L_{5100} = 44.98 - 46.19 \text{ erg s}^{-1}$) luminosities. Specifically, we used groups 1, 4, 7, and 10 and skipped the intermediate ones (2, 3, 5, 6, 8, and 9). This choice gives us the full dynamic range of the sample, while keeping the number of bins to a manageable number.

We do not increase the size of the bins to use all of the spectra in the sample because we are interested in creating high S/N composites of objects that are as similar as possible. The conversion of L_{5100} and H β FWHM into L/L_{Edd} and M_{BH} has significant uncertainties (e.g., Vestergaard & Peterson 2006; Shen et al. 2011). For example, high energy AGN spectral energy distributions change as a function of luminosity (e.g., Steffen et al. 2006), and so derived quantities such as bolometric luminosities (required for L/L_{Edd}) are likely not properly calibrated for all luminosities (Richards et al. 2006a).

We then use the measurements of H β from Shen et al. (2011) to separate objects into three groups: narrow, intermediate, and broad H β using 2000 and 4000 km s⁻¹ as our boundaries (excluding objects with H β FWHM > 20000 km s⁻¹). We choose fewer bins in H β FWHM compared to L_{5100} because of the considerably smaller dynamic range of the FWHM values, a factor of ≈ 20 compared to three orders of magnitude for the sample’s range of L_{5100} . The boundary at 2000 km s⁻¹ marks the traditional definition of narrow-line Seyfert 1s (Osterbrock & Pogge 1985), and the intermediate bin covers the main peak of the H β FWHM distribution.

Once the quasars are divided by luminosity and Balmer line width, we are interested in looking at the NLR properties of these bins. Specifically, we investigate if there is

¹ IRAF is distributed by the National Optical Astronomy Observatories, which are operated by the Association of Universities for Research in Astronomy, Inc., under cooperative agreement with the National Science Foundation.

² Hereafter when we refer to H β , we mean the broad component of the line from which a narrow-line component has been subtracted.

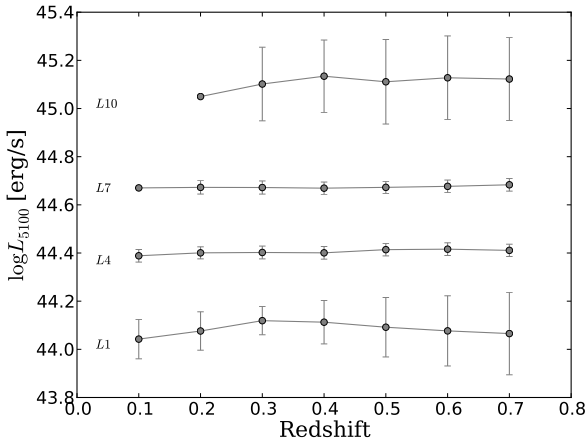


Figure 1. Median L_{5100} from Shen et al. (2011) vs. redshift. Within the given uncertainty, the continuum luminosity is constant within the same bin across redshift. The L_{10} group does not have objects with redshift < 0.2 . The error bars show the standard deviation in the bin. The two data points without error bars represent bins with fewer than 3 objects.

any evidence for redshift evolution that might be expected if AGN host galaxies have evolved since redshift 0.75. We thus divide each of these luminosity groups into 7 subsets according to their redshifts with bins of width 0.1 centred at: 0.1, 0.2, 0.3, 0.4, 0.5, 0.6, and 0.7. This results in $4 L_{5100} \times 3 H\beta \text{ FWHM} \times 7 z = 84$ bins, 8 of which are empty (primarily the high luminosity/low redshift ones) as shown in Table 1. For the 76 non-empty bins, we make median composite spectra with 3σ clipping using IRAF’s SCOMBINE tool. We choose to create median composites to preserve the EWs of the lines (see Vanden Berk et al. (2001) for a good discussion of the difference between median and mean composites).

To examine the distributions of objects within our binning, we look at the distributions of L_{5100} , $H\beta$ FWHM, and redshift (Fig. 1, 2, and 3). The figures show that the distributions are fairly consistent among the different bins. We note, however, that there are more quasars with higher luminosity at higher redshift as expected because of the SDSS flux limit for quasar spectroscopy ($i < 19.1$) and the redshift evolution of the quasar luminosity function (Richards et al. 2006b). Table 1 also shows that the narrow $H\beta$ subsets contain fewer objects than the intermediate and broad subsets. This is mainly due to the selection of objects in the SDSS quasar database requiring at least one broad line with $\text{FWHM} > 1000 \text{ km s}^{-1}$ (Schneider et al. 2010). The spectral library is given in Appendix A (available in the online-only version).

2.3 Measurements

Optical quasar spectra show several identifiable narrow emission lines. For this study, we focus on four narrow emission lines that are available in the wavelength range of our composites: $[\text{Ne V}] \lambda 3427$, $[\text{O II}] \lambda 3728$, $[\text{Ne III}] \lambda 3870$, and $[\text{O III}] \lambda 5007$, with ionization potentials of 97.1, 13.6, 40, 35 eV, respectively (Peterson 1997). These are the brightest, common emission lines, and they span a large range

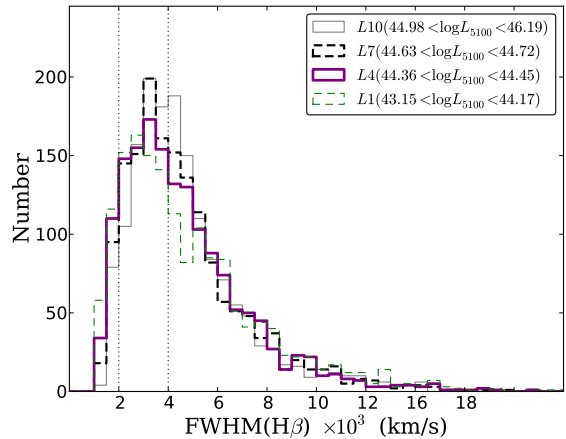


Figure 2. Distribution of $H\beta$ FWHM for the four luminosity subsets. The distributions look similar except for a weak trend of rising numbers of broader $H\beta$ objects in higher continuum luminosity bins (grey solid line). Narrower $H\beta$ quasars are more abundant in the lowest luminosity bin (green dashed line). Objects with $H\beta$ FWHM $> 20,000 \text{ km s}^{-1}$ are not included in making the composites as these were often found to arise from either bad measurements or low quality spectra.

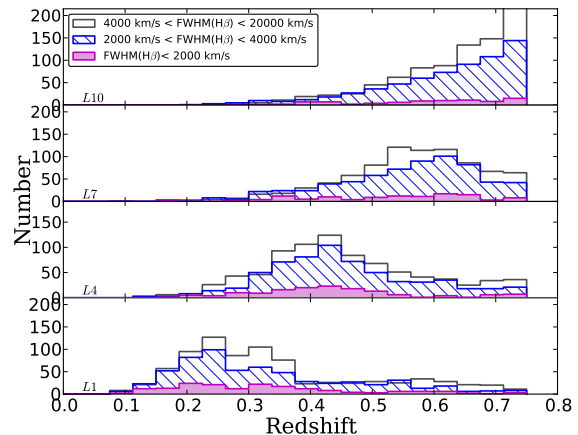


Figure 3. Distribution of redshift at the four continuum luminosity levels for the narrow (solid magenta), intermediate (hashed blue) and broad (open grey) $H\beta$ subsets. There is a gradual shift in the distributions of redshift from lower luminosity to the higher luminosity subsets – higher luminosity objects have more objects at higher redshift than lower luminosity ones as expected from the SDSS flux limit for quasar spectroscopy and the redshift evolution of the quasar luminosity function.

of ionization potentials. The high S/N present in most of our composites allows us to measure some of the relatively weak features such as $[\text{Ne III}] \lambda 3728$ that are typically not detected in individual spectra. We measure the flux of these narrow lines in each composite using one of two approaches. First, in the $H\beta - [\text{O III}] \lambda\lambda 4959, 5007$ region, we use IRAF’s SPECFIT package to fit the composite with a multicomponent model (Kriss 1994). This method allows us to subtract

Table 1. Breakdown of the number of objects in each luminosity subset with narrow (n; $\text{FWHM} < 2000 \text{ km s}^{-1}$), intermediate (i; $2000 \text{ km s}^{-1} < \text{FWHM} < 4000 \text{ km s}^{-1}$), and broad (b; $4000 \text{ km s}^{-1} < \text{FWHM} < 20,000 \text{ km s}^{-1}$) $\text{H}\beta$ at each redshift step. We only use the bins with > 10 objects to create composites. Those bins are highlighted with boldface in this table.

| $\log L_{5100}$ [erg s^{-1}] | L1 | | | L4 | | | L7 | | | L10 | | |
|---|---------------|-----|-----|---------------|----------|----------|---------------|----------|----------|---------------|----------|-----------|
| | 43.15 – 44.17 | | | 44.36 – 44.45 | | | 44.63 – 44.72 | | | 44.98 – 46.19 | | |
| Redshift | n | i | b | n | i | b | n | i | b | n | i | b |
| 0.1 | 14 | 29 | 29 | 0 | 3 | 1 | 0 | 0 | 1 | 0 | 0 | 0 |
| 0.2 | 55 | 203 | 249 | 10 | 20 | 23 | 1 | 7 | 9 | 0 | 0 | 1 |
| 0.3 | 40 | 168 | 255 | 22 | 92 | 126 | 6 | 36 | 28 | 2 | 19 | 10 |
| 0.4 | 34 | 75 | 91 | 56 | 238 | 299 | 27 | 81 | 85 | 16 | 37 | 49 |
| 0.5 | 12 | 72 | 68 | 34 | 141 | 188 | 19 | 143 | 216 | 8 | 94 | 108 |
| 0.6 | 13 | 38 | 82 | 8 | 85 | 104 | 37 | 252 | 306 | 27 | 178 | 232 |
| 0.7 | 6 | 21 | 41 | 14 | 51 | 84 | 23 | 137 | 184 | 30 | 314 | 475 |
| Total | 174 | 606 | 815 | 144 | 630 | 825 | 113 | 656 | 830 | 83 | 642 | 875 |

the Fe II emission features which form a pseudo-continuum of blended lines that are in some cases heavily blended with other emission lines in this part of the spectrum. For the removal of the Fe II lines, we make use of the Fe II template of [Véron-Cetty, Joly & Véron \(2004\)](#). We use a Lorentzian and up to two Gaussians to fit $\text{H}\beta$, and up to three Gaussians to fit each of the [O III] lines. An example of the fitting model in this spectral region is shown in Figure 4. In the [Ne III] - [Ne V] - [O II] ($\sim 3300 - 4000 \text{ \AA}$) region we use IRAF’s SPLOT tool and simply integrate the flux above the continuum (defined around the emission line by visual inspection) as we do not anticipate significant contamination from the Fe II lines.

The results of the measurements are tabulated in Table 3.

We use the L_{5100} and $\text{H}\beta$ width measurements to calculate the BH mass and accretion rate for each composite. For the BH masses, we use equation 5 from [Vestergaard & Peterson \(2006\)](#):

$$\log \frac{M_{BH}}{M_{\odot}} = 0.910 + 0.5 \log \left(\frac{5100 L_{5100}}{10^{44} \text{ erg s}^{-1}} \right) + 2 \log \left(\frac{\text{FWHM}(\text{H}\beta)}{\text{km s}^{-1}} \right). \quad (1)$$

For the accretion rates, we estimate the bolometric luminosity as $L_{\text{bol}} = 9 L_{5100}$ ([Peterson 1997](#)). The Eddington luminosity, L_{Edd} , is calculated as ([Netzer 2006](#)):

$$L_{\text{Edd}} \simeq 1.5 \times 10^{38} \left(\frac{M_{BH}}{M_{\odot}} \right) \text{ erg s}^{-1}. \quad (2)$$

Values of the calculated M_{BH} , L_{Edd} , and L_{bol} for each composite are given in Table 2. [Richards et al. \(2006a\)](#) have expressed some reservations about the potential pitfalls of applying a single bolometric correction to all quasars as it is quite likely that different quasar populations should have distinct bolometric correction values because of systematic differences in their spectral energy distributions ([Krawczyk et al. 2013](#)). This concern was among the reasons that the samples comprising each composite are binned by L_{5100} and $\text{H}\beta$ width alone rather than the derived quantities of M_{BH} and L/L_{Edd} . We emphasize that these reported values of M_{BH} , L_{Edd} , and L_{bol} are not used for the binning of objects for the composite selection, but are simply reported for completeness.

Table 2. BH masses, L_{bol} and L_{Edd} for the composites in each of the L_{5100} and $\text{H}\beta$ width bins.

| Composite | $\log(M_{BH}/M_{\odot})$ | $\log L_{\text{Edd}}$ [erg s^{-1}] | $\log L_{\text{bol}}$ [erg s^{-1}] | L/L_{Edd} |
|-----------|--------------------------|---|---|--------------------|
| nL1 | 7.39 | 45.57 | 45.06 | 0.31 |
| iL1 | 7.90 | 46.08 | 45.05 | 0.09 |
| bL1 | 8.54 | 46.71 | 45.05 | 0.02 |
| nL4 | 7.57 | 45.75 | 45.37 | 0.41 |
| iL4 | 8.00 | 46.18 | 45.36 | 0.15 |
| bL4 | 8.63 | 46.81 | 45.36 | 0.04 |
| nL7 | 7.73 | 45.90 | 45.63 | 0.53 |
| iL7 | 8.22 | 46.40 | 45.63 | 0.17 |
| bL7 | 8.74 | 46.92 | 45.63 | 0.05 |
| nL10 | 7.98 | 46.16 | 46.06 | 0.80 |
| iL10 | 8.47 | 46.64 | 46.08 | 0.28 |
| bL10 | 8.94 | 47.12 | 46.07 | 0.09 |

3 MEASURED LINE LUMINOSITIES

The table below (Table 3) includes the measured line luminosities for the four narrow lines discussed in this paper ([Ne V], [Ne III], [O II], and [O III]). The full table is available online as an electronic table.

4 RESULTS AND DISCUSSION

4.1 Line Luminosity and Redshift

We focus on the four strongest forbidden lines present in the spectral range of our composites: [Ne V] $\lambda 3427$, [Ne III] $\lambda 3870$, [O III] $\lambda 5007$, and [O II] $\lambda 3728$. In addition, we only use the spectra constructed from more than 10 objects. We trace these four lines across redshift through their luminosities and flux ratios in each of the 7 $L_{5100}/\text{FWHM}(\text{H}\beta)$ bins. In a stratified NLR and with IPs spreading over a range of $\sim 13 - 100 \text{ eV}$, we expect the lines with low IP (e.g. [O II]; IP = 13.5 eV) to be emitted farther away from the SMBH (and thus the source of the ionizing continuum) and therefore from regions with weaker AGN influence than the high IP lines (e.g. [Ne V]; IP = 97 eV).

As mentioned in §2.2, the selection of objects that went into each of the composites is not dependent on any properties of the NLR. In addition, by dividing the spectra into

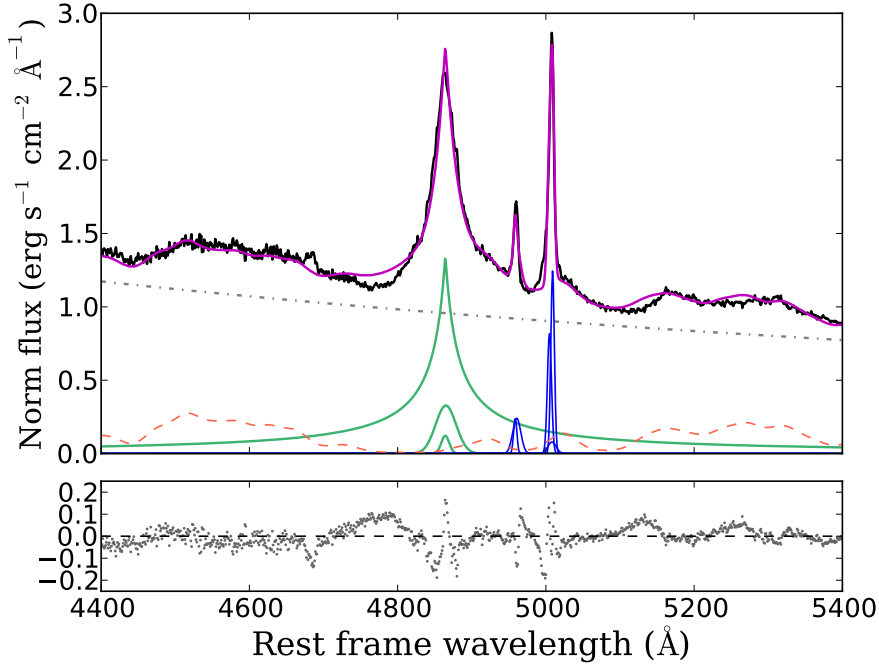


Figure 4. Model fit for composite iL7z2 (black) and the full fitting result (magenta). $H\beta$ is fit with a Lorentzian and up to two Gaussians (green), the $[O\text{ III}]$ doublet is fit with up to three Gaussians per line (blue), the grey dash-dot line is a power-law continuum, and the Fe II template is shown as a dashed red line. The residuals are shown in the lower panel.

Table 3. Measured line luminosities for the four forbidden lines $[O\text{ II}]$, $[O\text{ III}]$, $[\text{Ne III}]$, and $[\text{Ne V}]$. The full table is available online as an electronic table.

| Composite | z | $L([\text{Ne V}])$ $\times 10^{40} \text{erg s}^{-1}$ | $L([\text{Ne III}])$ $\times 10^{40} \text{erg s}^{-1}$ | $L([O\text{ II}])$ $\times 10^{40} \text{erg s}^{-1}$ | $L([O\text{ III}])$ $\times 10^{40} \text{erg s}^{-1}$ |
|-----------|-----|--|--|--|---|
| nL1z1 | 0.1 | 17.08 ± 0.79 | 5.55 ± 0.51 | 7.29 ± 0.50 | 23.68 ± 5.97 |
| nL1z2 | 0.2 | 9.88 ± 0.41 | 6.68 ± 0.45 | 9.49 ± 0.39 | 21.71 ± 4.62 |
| nL1z3 | 0.3 | 10.18 ± 0.78 | 11.02 ± 0.77 | 12.25 ± 0.72 | 21.09 ± 1.14 |
| nL1z4 | 0.4 | 11.74 ± 0.96 | 13.11 ± 0.99 | 12.62 ± 0.81 | 25.56 ± 1.65 |
| nL1z5 | 0.5 | 7.95 ± 1.99 | 5.61 ± 1.70 | 14.93 ± 2.07 | 34.09 ± 2.07 |
| nL1z6 | 0.6 | 18.03 ± 5.41 | 15.21 ± 5.60 | 22.80 ± 4.55 | 72.31 ± 7.37 |
| nL1z7 | 0.7 | 28.98 ± 9.22 | 8.27 ± 8.06 | 17.77 ± 7.73 | 89.13 ± 17.34 |

bins of L_{5100} and $H\beta$ FWHM, we aim to ensure that the objects used in making each composite are powered by similar central sources in the sense that the continuum luminosity and the $H\beta$ FWHM are sensitive to the L/L_{Edd} ratios and BH masses of quasars. We choose *not* to use the derived values of Eddington ratio and M_{BH} , but rather the measured values of 5100 Å luminosity and FWHM $H\beta$ as these are straightforward spectral measurements that are not subject to changes in calibration or uncertain assumptions about bolometric corrections.

Figure 5 shows the line luminosities for the four lines plotted against redshift. Visually, we see a weak overall tendency of the luminosities of the lower IP lines to increase towards higher redshifts. To examine this apparent trend more quantitatively, we calculate the slopes of the line luminosity vs. redshift for each L_{5100} and $H\beta$ bins along with the correlation coefficients (Table 4). We discuss the lines individually in the following subsections.

4.1.1 $L([O\text{ II}])$

Compared to the much more prominent $[O\text{ III}]$, the $[O\text{ II}]$ line is fairly weak in the spectra of radio-quiet quasars. In general, $[O\text{ II}]$ emission may have contributions from photoionization from the AGN and/or star-formation in the host galaxy. Photoionization models suggest that in a pure AGN, the $[O\text{ II}]$ to $[O\text{ III}]$ ratio ranges between 0.1 and 0.3 (Ho 2005, and references therein). Similarly, Kim, Ho & Im (2006) find that in quasars, the AGN contribution to $[O\text{ II}]$ is more dominant than the host galaxy's. The $[O\text{ II}]$ luminosities in our composite spectra are shown in top-left panel of Figure 5. The figure shows a trend of increasing $[O\text{ II}]$ luminosity with redshift of nearly an order of magnitude. We calculated a Spearman correlation coefficient of $\rho_S = 0.54$ for $[O\text{ II}]$ luminosity vs. redshift shown in Figure 5, with $p < 0.0001$ (p being the probability of no correlation) which indicates the high probability that the two quantities are strongly cor-

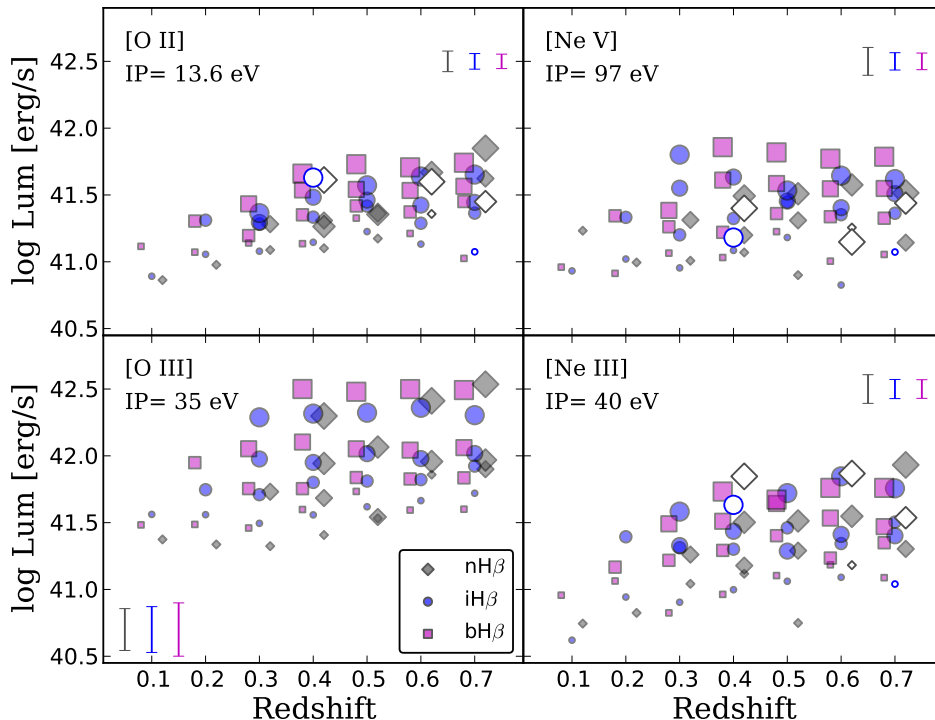


Figure 5. Line luminosity vs. redshift for the four narrow lines. Grey diamonds are the composites with $H\beta < 2000 \text{ km s}^{-1}$, blue circles are the composites with $2000 < H\beta < 4000 \text{ km s}^{-1}$, and magenta squares are the composites with $4000 \text{ km s}^{-1} < H\beta < 20000 \text{ km s}^{-1}$. Open symbols denote non-detections. Marker size corresponds to the continuum luminosity bin: larger for higher L_{5100} . Only composites with $N > 10$ are included. The grey/magenta points are slightly offset to the left/right of their redshift value for clarity. In all luminosity bins, the [O II] line is clearly becoming stronger at higher redshifts. The overall Spearman test gave: $\rho_S([\text{O II}]) = 0.532$, $p = 0.000$; $\rho_S([\text{O III}]) = 0.447$, $p = 0.000$; $\rho_S([\text{Ne III}]) = 0.479$, $p = 0.000$; $\rho_S([\text{Ne V}]) = 0.373$, $p = 0.005$ for about 60 objects (detections only).

related. We note however that this correlation can potentially be a result of the missing high luminosity, low-redshift quasar composites in our sample. However, tracing the data from quasars of similar luminosity, the general trend is towards higher [O II] luminosities at higher redshift. To further examine this possibility, we look at the correlation between the line luminosity and redshift for each L_{5100} bin separately and we find that the correlation is still strong for most cases but the significance of the correlation becomes much lower (higher p value) as a result of fewer data points in each subsample (L1: $\rho_S = 0.510$, L4: $\rho_S = 0.736$, L7: $\rho_S = 0.385$, L10: $\rho_S = 0.608$). In addition to the Spearman test, we calculate a least-squares regression slope for each L_{5100} and $H\beta$ bin (Table 4) and find that in most cases, [O II] has a weak but significant trend to increase towards higher redshift.

The [O II] luminosity is indeed known to be a reliable tracer of SFR in non-AGN and AGN galaxies (e.g. Gallagher, Hunter & Bushouse 1989; Kennicutt 1998; Rosa-González, Terlevich & Terlevich 2002; Hopkins et al. 2003; Kewley, Geller & Jansen 2004; Ho 2005; Kim, Ho & Im 2006; Silverman et al. 2009). This line becomes particularly important for samples with $z \geq 0.5$ as the primary SFR metric of $H\alpha$ has passed out of the optical bandpass (e.g. Kewley, Geller & Jansen 2004). To get a handle on whether star formation might be contributing to the [O II] emission, we

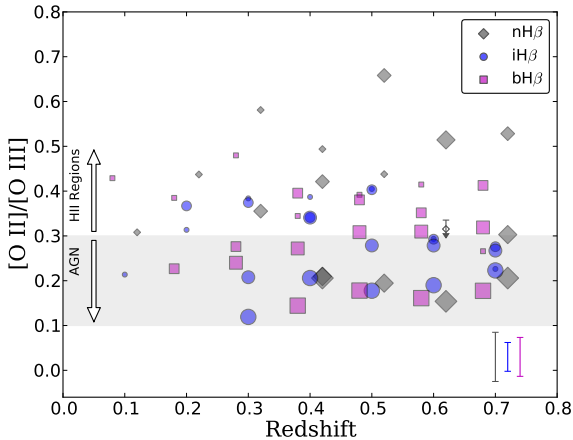
consider the ratio of the line fluxes of the two oxygen lines. Figure 6 shows the flux ratio of [O II] to [O III] in our sample. The figure shows that almost 50% of the objects (primarily among the low and intermediate continuum luminosity bins; $\log L_{5100} \sim 43 - 44.5 \text{ erg s}^{-1}$) have $[\text{O II}]/[\text{O III}] > 0.3$ consistent with [O II] emission produced in stellar H II regions (Osterbrock & Ferland 2006). Therefore, we conclude that there is a contribution from star formation to the [O II] emission, at least in some objects.

The apparent increase in [O II] line luminosity as a function of redshift could arise from different factors other than an increase in SFR in the typical quasar host galaxy. For instance, the use of a fixed-size aperture (the SDSS uses a $3''$ fiber) means that spectra potentially include a larger fraction of the host galaxy gas at high redshifts than in lower redshift objects due to the larger projected physical size at higher redshifts. Specifically, the projected size is 5.5 kpc at $z = 0.1$ and 22 kpc at $z = 0.7$. However, we do not anticipate this to be the main reason for the observed increase in the [O II] luminosity (if due solely to photo-ionization by the quasar) as the size of the entire NLR is probably less than 10 kpc. To check, we employ the NLR scaling relation from Bennert et al. (2002, their eq. 1):

$$\log R_{NLR} = (0.52 \pm 0.006) \log L_{[\text{O III}]} - (18.5 \pm 2.6), \quad (3)$$

Table 4. Results of the least-squares regression and the Spearman rank coefficient for the line luminosities and redshift for the four narrow-lines in each of the 7 L_{5100} and $H\beta$ bins.

| Subset | Line | Slope | Std Error | ρ_S | p |
|-----------------------------|----------|--------|-----------|----------|--------|
| nHβ | [O II] | 1.281 | 0.222 | 0.702 | 0.0008 |
| | [O III] | 1.400 | 0.412 | 0.497 | 0.0171 |
| | [Ne III] | 1.430 | 0.366 | 0.450 | 0.0309 |
| | [Ne V] | 0.473 | 0.348 | 0.196 | 0.3811 |
| iHβ | [O II] | 0.509 | 0.223 | 0.380 | 0.0625 |
| | [O III] | 0.567 | 0.316 | 0.399 | 0.0505 |
| | [Ne III] | 0.746 | 0.331 | 0.448 | 0.0282 |
| | [Ne V] | 0.494 | 0.322 | 0.120 | 0.5571 |
| bHβ | [O II] | 0.550 | 0.249 | 0.543 | 0.0056 |
| | [O III] | 0.679 | 0.398 | 0.172 | 0.3804 |
| | [Ne III] | 0.695 | 0.315 | 0.378 | 0.0536 |
| | [Ne V] | 0.633 | 0.340 | 0.378 | 0.0542 |
| L1 | [O II] | 0.297 | 0.114 | 0.510 | 0.026 |
| | [O III] | 0.459 | 0.120 | 0.708 | 0.000 |
| | [Ne III] | 0.524 | 0.127 | 0.727 | 0.001 |
| | [Ne V] | 0.014 | 0.147 | 0.088 | 0.729 |
| L4 | [O II] | 0.376 | 0.110 | 0.736 | 0.001 |
| | [O III] | 0.176 | 0.149 | 0.450 | 0.080 |
| | [Ne III] | 0.238 | 0.133 | 0.443 | 0.086 |
| | [Ne V] | 0.033 | 0.121 | 0.209 | 0.438 |
| L7 | [O II] | 0.343 | 0.199 | 0.385 | 0.174 |
| | [O III] | -0.003 | 0.104 | 0.029 | 0.921 |
| | [Ne III] | 0.109 | 0.188 | 0.188 | 0.519 |
| | [Ne V] | 0.016 | 0.167 | -0.045 | 0.884 |
| L10 | [O II] | 0.588 | 0.195 | 0.608 | 0.036 |
| | [O III] | 0.310 | 0.197 | 0.462 | 0.131 |
| | [Ne III] | 0.464 | 0.183 | 0.626 | 0.029 |
| | [Ne V] | -0.451 | 0.297 | -0.607 | 0.083 |


Figure 6. $[O II]/[O III]$ flux ratio plotted against redshift. Markers are similar to Fig. 5. The shaded region marks the 0.1–0.3 boundary for an AGN-dominated line ratio; a ratio larger than 0.3 is typical of stellar H II regions). The line ratio distribution shows no evidence for evolution as a function of redshift.

and our measured $[O III]$ luminosities (which are significantly higher than the $[O II]$ luminosities), we find the size of the NLR in our composites is ~ 4 kpc. If the $[O II]$ emission is

instead largely from star formation in the host galaxy, then the size of the star-forming region within the galaxy is the relevant factor. However, the size of the entire galaxy is not expected to exceed ~ 10 kpc, and the star-forming regions may be considerably more compact. Ichikawa, Kajisawa & Akhlaghi (2012), for example, found in a sample of galaxies selected from the MOIRCS Deep Survey with up to redshift 3, that the half-light radius (R_{50}) in the K -band is between 5–10 kpc.

The calculation of SFRs using the $[O II]$ line in isolation is, however, not completely straightforward. The conversion of the observed line luminosity to SFRs is complicated by effects such as reddening and metal abundance. Several attempts have been made to come up with calibrations that allow for a direct estimation of SFRs from line fluxes (e.g., Rosa-González, Terlevich & Terlevich 2002; Kewley, Geller & Jansen 2004). These calibrations are useful for estimating SFRs without directly involving assumptions about metallicity and intrinsic extinction that are by and large the major sources of uncertainty. We use the $L([O II])$ calibration equation from Rosa-González, Terlevich & Terlevich (2002) for non-AGN galaxies to estimate SFRs for our composite spectra:

$$SFR_{[O II]} = 8.4 \times 10^{-41} L_{[O II]} M_{\odot} \text{yr}^{-1}, \quad (4)$$

where we have first subtracted 10% of the $[O III]$ luminosity

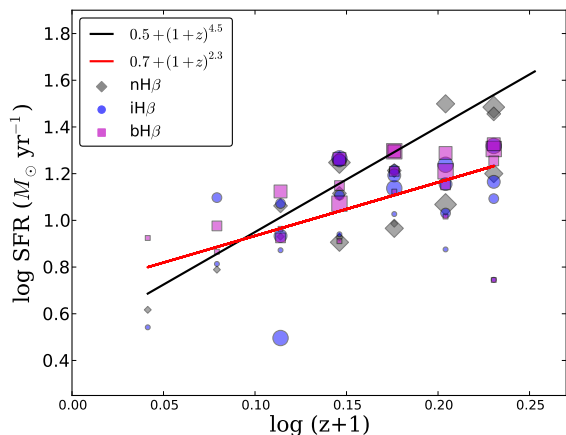


Figure 7. SFRs estimated with Eq. 4. The points are color-coded to show the narrow H β composites in grey, intermediate in blue, and broad in magenta. Larger stars indicate higher L_{5100} bins. The solid black line is $(1+z)^{4.5} + 0.5$ from Rosa-González, Terlevich & Terlevich (2002) and the red line is our fit with a slope of 2.3 ± 0.4 and intercept of 0.7. The figure shows a clear increase in the estimated SFRs towards higher redshift, though our sample shows less evolution than the non-AGN galaxy sample.

from the [O II] luminosity to account for the AGN contribution, i.e., we have assumed all of the [O III] emission is from the AGN, and assumed an [O II] to [O III] line ratio of 0.1. We plot the results in Figure 7 which shows that the SFR calculated with equation 4 increases with z . As interpreted at face value, the figure also shows that higher continuum luminosity composites have higher SFRs as expected from the higher [O II] luminosities in the higher L_{5100} composites (see Fig. 5). The different H β FWHM bins overlap in terms of SFRs. We are also interested in comparing the slope of SFR vs. z for our sample and a sample of non-AGN galaxies. Rosa-González, Terlevich & Terlevich (2002) found a best fit for the $z = 0-1$ range of $SFR \propto (1+z)^{4.5}$; the line representing this fit is shown in Fig. 7 (with an offset of 0.5 to match our data). Our best fit is also shown in the figure with a slope of 2.3 ± 0.4 which is notably smaller than the Rosa-González, Terlevich & Terlevich (2002) fit. Given the assumptions that have gone into converting our [O II] luminosities (which have an uncertain contribution from the quasar) into SFRs, it is not clear that this indicates a significant discrepancy between the samples.

4.1.2 The AGN Lines

With higher IPs, the [O III], [Ne III], and [Ne V] lines can be thought of as AGN lines (IPs: 35, 40, and 97 eV, respectively). After accounting for the lack of high luminosity, low redshifts sources, the luminosities of [Ne III] and [O III] are almost constant with redshift as the two lower panels of Figure 5 show. With almost equal IPs of 35 and 40 eV, [O III] and [Ne III] are both expected to respond similarly to the ionizing radiation and consequently have similar behaviour across redshift.

We calculate Spearman correlation coefficients for each line vs. redshift and find: $\rho_S([\text{O III}]) = 0.447$ ($p < 0.0001$), $\rho_S([\text{Ne III}]) = 0.479$ ($p < 0.0001$). The slight increase in

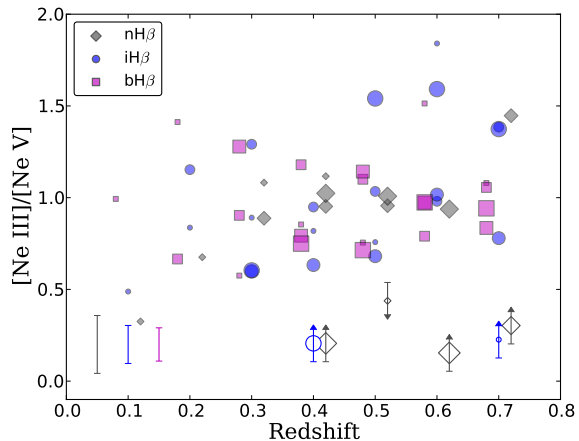


Figure 8. [Ne III]/[Ne V] flux ratio. The ratio does not show a clear trend with redshift indicating no evidence for a change in the ionizing spectrum with redshift.

the luminosities of these two lines might be a result of the contribution of the host galaxy ISM which undergoes enhanced SFRs at higher redshift. However, a comparison of the apparent increase in [O III] luminosity with redshift to the error bars (lower left corner of Fig. 5), and tracing the trend within each luminosity bin indicates to us that this apparent correlation is not real.

As for the [Ne V] line (Fig. 5), the correlation is still significant but is much weaker with $\rho_S([\text{Ne V}]) = 0.373$ ($p = 0.005$). Table 4 lists all the slopes and the Spearman correlation coefficients calculated for the luminosity and H β bins separately for the line luminosity vs. redshift correlations.

This again supports the notion of a pure AGN line with luminosity that is not changing up to redshift 0.75. The behaviour of [Ne V] is as expected in a scenario where the ionizing radiation (and consequently the ionization parameter) is not changing over redshift. The [Ne III]/[Ne V] flux ratio shown in Fig. 8 does indeed show evidence for no change in the hardness of the ionizing radiation in the redshift range of 0–0.75.

4.2 [O III], Fe II and Eigenvector 1

A suite of correlations among quasar spectral properties have been identified, most notably from Principal Component Analysis (PCA) (e.g. Boroson & Green 1992; Boroson 2002; Sulentic et al. 2007). One strong PCA correlation that is particularly related to the spectral range we are focusing on is referred to as Eigenvector 1 (EV1; Boroson & Green 1992; Boroson 2002). EV1 describes an inverse correlation between the strengths of [O III] $\lambda 5007$ and the Fe II $\lambda 4570$ feature (the strength of Fe II is often quantified as the EW ratio of Fe II to H β , defined as R_{FeII}). In addition to [O III] and Fe II, EV1 also includes correlations among quantities such as H β width, line blueshift and asymmetry, and the radio-loudness (e.g. Bachev et al. 2004). This is usually seen as objects with strong Fe II have weaker [O III], narrower, symmetric H β , and are more likely to be radio-quiet. In Fig. 9, we plot the [O III] luminosity and EW vs. R_{FeII} . The R_{FeII} values in this figure are derived from the median values of

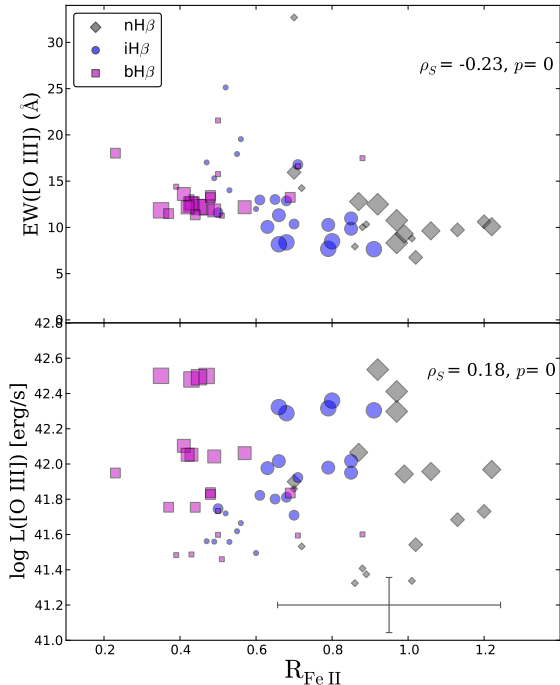


Figure 9. Top: The [O III] EW is plotted against the $R_{\text{Fe II}}$ ratio. The marker shapes correspond to $H\beta$ width (as labeled in the legend) and the sizes are proportional to the L_{5100} bin. The two quantities are strongly anti-correlated with $\rho_S = -0.63$. Bottom: [O III] luminosity plotted against $R_{\text{Fe II}}$. Average error bars are shown. The two quantities appear to be uncorrelated with $\rho_S = 0.18$.

the $H\beta$ and Fe II from the Shen et al. (2011) measurements. Figure 9 shows that composites with narrower $H\beta$ do indeed have stronger Fe II. Our composite spectra (see Appendix A in the online version) also show that objects with narrower $H\beta$ have stronger, more conspicuous Fe II. Figure 9 (top panel) also shows that the [O III] EW and the $R_{\text{Fe II}}$ ratio are anti-correlated –in agreement with the EV1 findings. We also examine the correlation between the [O III] and Fe II using the [O III] line luminosity (Fig. 9, lower panel) but we find no correlation between the two quantities. We note that the original EV1 studies (Boroson & Green 1992; Boroson 2002) used the equivalent width of [O III] (or its ratio to the $H\beta$ line) to quantify its strength rather than the luminosity. The [O III] and the Fe II lines are emitted in two regions with different physical properties (e.g. density and ionization parameter) and at significantly different size scales (i.e., kpcs vs. pcs). Despite being repeatedly found, the presence of a correlation between these two lines has not been fully understood. The predominant factor that appears to be driving this correlation is the accretion rate (Boroson & Green 1992; Boroson 2002; Shen & Ho 2014). In this picture, objects at high accretion rates have thicker accretion disks which blocks radiation from reaching the narrow-line region leading to weaker [O III] emission, however, this scenario does not account for the correlation that include Fe II.

5 SUMMARY AND CONCLUSION

In this work we examine the narrow forbidden lines in quasar optical spectra across redshift and up to $z = 0.75$. To enhance the S/N, we utilize a large sample of quasars from the SDSS-DR7 and create 62 median composite spectra (with at least 10 objects in each composite). We indirectly constrain the properties of the central source (accretion rate and BH mass) by grouping objects with similar L_{5100} and $H\beta$ values in bins that we use to make the composites.

Our results can be summarized as follows:

(i) The luminosity of the lowest ionization narrow line, [O II], appears to increase with redshift (top-left panel of Fig. 5). Because the [O II] line is known to be a reliable SFR estimator in non-active galaxies, we interpret this result as evidence for higher SFRs in the host galaxies of AGNs at higher redshift. We calculate a SFR using the [O II] luminosity and the scaling relation of Rosa-González, Terlevich & Terlevich (2002) and find that the estimated SFR is increasing with redshift however with a smaller power-law slope (2.3 ± 0.4) than found in non-AGN galaxies (4.5 ; Rosa-González, Terlevich & Terlevich 2002).

(ii) The strength of the correlation between the line luminosity and redshift appears to depend on the IP of the line. The luminosity of the line with the lowest IP ([O II]) has the strongest correlation with redshift while the “intermediate” IP lines ([Ne III] and [O III]) have weaker dependencies and the [Ne V] with IP = 97 eV appears to be independent of redshift (Fig. 5, see also Table 4). This behaviour is in line with the idea of a stratified NLR where lines with higher IPs are emitted closer to the central source (which is similar for $z < 0.75$) with negligible contribution from the host galaxy gas while lines with low IPs are emitted farther out and also have more contribution from stellar sources of ionizing radiation.

(iii) We find that the strength of the broad Fe II emission is anti-correlated with both the [O III] EW and the width of $H\beta$, i.e., objects with weaker [O III] (lower EWs) tend to have narrower $H\beta$ and stronger Fe II (larger $R_{\text{Fe II}}$, see Fig. 9). This result is in agreement with the definition of EV1 (Boroson & Green 1992; Boroson 2002). The presence of a correlation between these lines has been attributed to the accretion rate of the central source (L/L_{Edd}).

The study of the impact of AGNs on their host galaxies allows us to probe galaxy evolution and the possible role that SMBHs play in it. AGN narrow-line regions are the zones where the interaction between the ionizing radiation from the accretion disk and the host galaxy ISM takes place and can therefore serve as excellent probes of the AGN–host galaxy interface. The increase in the SFRs at higher redshift (up to $z \sim 1-2$) is well-known in non-AGN galaxies and appears to show similar behaviour in AGN hosts. Examining higher redshifts to explore this trend further will require near-IR spectroscopy.

ACKNOWLEDGMENTS

We are grateful to to Françoise Combes and Niel Brandt for thoughtful discussions. This work was supported by the Schlumberger Foundation - Faculty for the Future Program

(A.T.), the Natural Science and Engineering Research Council of Canada, and the Ontario Early Researcher Award Program (A.T., S. C. G.). This research made use of Astropy, a community-developed core Python package for Astronomy (Astropy Collaboration et al. 2013). Funding for the SDSS and SDSS-II has been provided by the Alfred P. Sloan Foundation, the Participating Institutions, the National Science Foundation, the U.S. Department of Energy, the National Aeronautics and Space Administration, the Japanese Monbukagakusho, the Max Planck Society, and the Higher Education Funding Council for England. The SDSS Web Site is <http://www.sdss.org/>. We thank the anonymous referee for helpful comments that improved this paper.

REFERENCES

- Antonucci R., 1993, *ARA&A*, 31, 473
 Astropy Collaboration et al., 2013, *A&Ap*, 558, A33
 Bachev R., Marziani P., Sulentic J. W., Zamanov R., Calvani M., Dultzin-Hacyan D., 2004, *AJ*, 617, 171
 Bennert N., Falcke H., Schulz H., Wilson A. S., Wills B. J., 2002, *ApJL*, 574, L105
 Boroson T. A., 2002, *AJ*, 565, 78
 Boroson T. A., Green R. F., 1992, *ApJS*, 80, 109
 Croom S. M. et al., 2002, *MNRAS*, 337, 275
 Gallagher J. S., Hunter D. A., Bushouse H., 1989, *ApJ*, 97, 700
 Hewett P. C., Wild V., 2010, *MNRAS*, 405, 2302
 Hill A. R., Gallagher S. C., Deo R. P., Peeters E., Richards G. T., 2014, *MNRAS*, 438, 2317
 Ho L. C., 2005, *AJ*, 629, 680
 Hopkins A. M. et al., 2003, *AJ*, 599, 971
 Ichikawa T., Kajisawa M., Akhlaghi M., 2012, *MNRAS*, 422, 1014
 Jester S. et al., 2005, *ApJ*, 130, 873
 Kennicutt, Jr. R. C., 1998, *ARA&A*, 36, 189
 Kewley L. J., Geller M. J., Jansen R. A., 2004, *ApJ*, 127, 2002
 Kim M., Ho L. C., Im M., 2006, *AJ*, 642, 702
 Krawczyk C. M., Richards G. T., Mehta S. S., Vogeley M. S., Gallagher S. C., Leighly K. M., Ross N. P., Schneider D. P., 2013, *ApJS*, 206, 4
 Kriss G., 1994, *Astronomical Data Analysis Software and Systems*, 3, 437
 Netzer H., 2006, in *Lecture Notes in Physics*, Berlin Springer Verlag, Vol. 693, *Physics of Active Galactic Nuclei at all Scales*, Alloin D., ed., p. 1
 Osterbrock D. E., Ferland G. J., 2006, *Astrophysics of gaseous nebulae and active galactic nuclei*
 Osterbrock D. E., Pogge R. W., 1985, *AJ*, 297, 166
 Peterson B. M., 1997, *An Introduction to Active Galactic Nuclei*
 Richards G. T. et al., 2006a, *ApJS*, 166, 470
 Richards G. T. et al., 2006b, *ApJ*, 131, 2766
 Rosa-González D., Terlevich E., Terlevich R., 2002, *MNRAS*, 332, 283
 Schneider D. P. et al., 2010, *ApJ*, 139, 2360
 Shakura N. I., Sunyaev R. A., 1973, *A&Ap*, 24, 337
 Shen Y., Ho L. C., 2014, *Nature*, 513, 210
 Shen Y. et al., 2011, *ApJS*, 194, 45
 Silverman J. D. et al., 2009, *AJ*, 696, 396
 Spergel D. N. et al., 2003, *ApJS*, 148, 175
 Steffen A. T., Strateva I., Brandt W. N., Alexander D. M., Koekemoer A. M., Lehmer B. D., Schneider D. P., Vignali C., 2006, *ApJ*, 131, 2826
 Sulentic J. W., Bachev R., Marziani P., Negrete C. A., Dultzin D., 2007, *AJ*, 666, 757
 Sulentic J. W., Marziani P., Zamanov R., Bachev R., Calvani M., Dultzin-Hacyan D., 2002, *ApJL*, 566, L71
 Urry C. M., Padovani P., 1995, *PASP*, 107, 803
 Vanden Berk D. E. et al., 2001, *ApJ*, 122, 549
 Véron-Cetty M.-P., Joly M., Véron P., 2004, *A&Ap*, 417, 515
 Vestergaard M., Peterson B. M., 2006, *AJ*, 641, 689
 Wild V., Hewett P. C., 2010, *ArXiv e-prints*

APPENDIX A: QUASAR SPECTRAL LIBRARY

This spectral library consists of 62 quasar spectra generated from a homogeneous set of quasars that share similar continuum luminosity, broad line width, and are at similar redshifts. Starting from a sample of $\sim 16,000$ quasars, we separate the objects into 4 groups of continuum luminosity (high, two intermediate, and low) and further separate each of these luminosity groups into 3 groups depending on their $H\beta$ width (using 2000 and 4000 kms^{-1} as boundaries). We further bin these groups at redshift steps of 0.1, 0.2, 0.3, 0.4, 0.5, 0.6, and 0.7. **The results are shown below. A full coloured version of the figures as well as the FITS files are available online.**

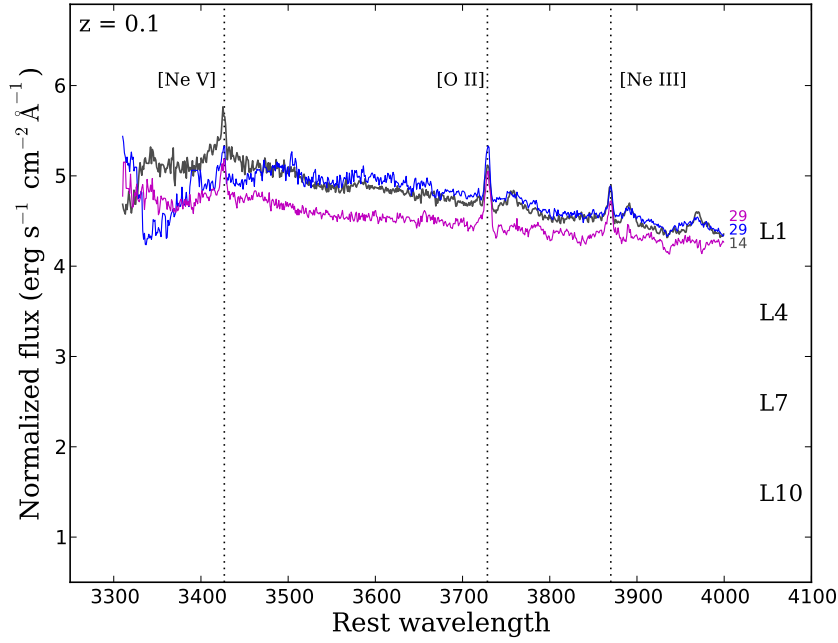


Figure A1. Median composite spectra at redshift $z=0.1$. Top is the high continuum luminosity (L10) and bottom is the low luminosity (L1). Spectra at the same luminosity level but with different widths of $H\beta$ are overplotted with narrow $H\beta$ in grey, intermediate $H\beta$ in blue, and broad $H\beta$ in magenta. To the right side, we show the number of individual spectrum used in making each composite. Only composites with > 10 objects are shown. L1, L4, L7 and L10 indicate the continuum luminosity subsets with L1 being the lowest and L10 the highest. At $z = 0.1$, only the lowest luminosity bin has data.

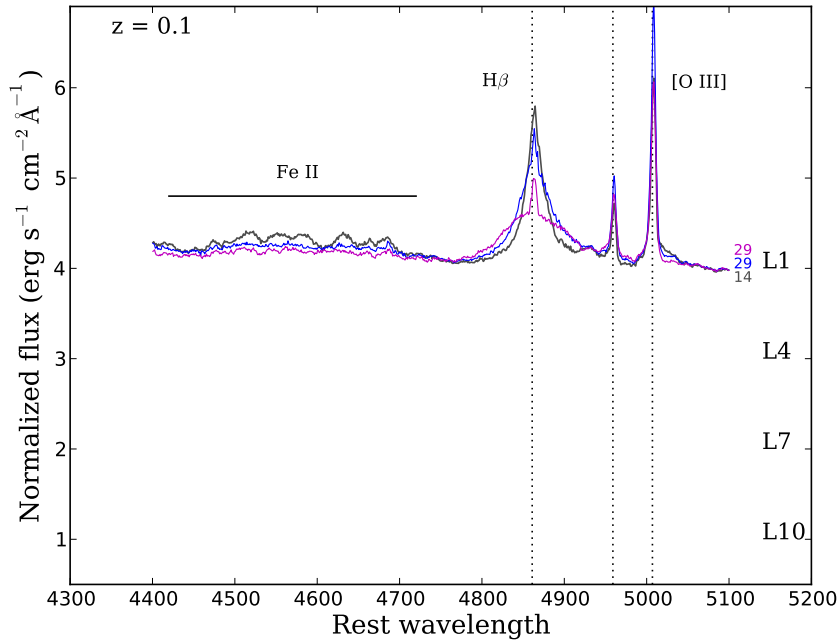


Figure A2. Similar to Fig. A but for the wavelength range covering $H\beta$ and $[O III]$.

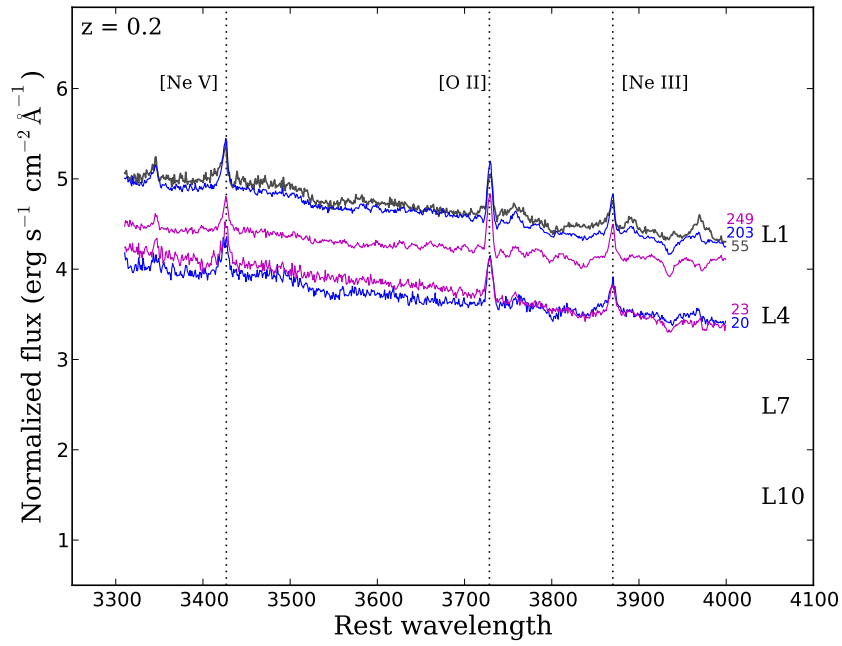


Figure A3. Same as Fig. A but for redshift bin centred at z= 0.2.

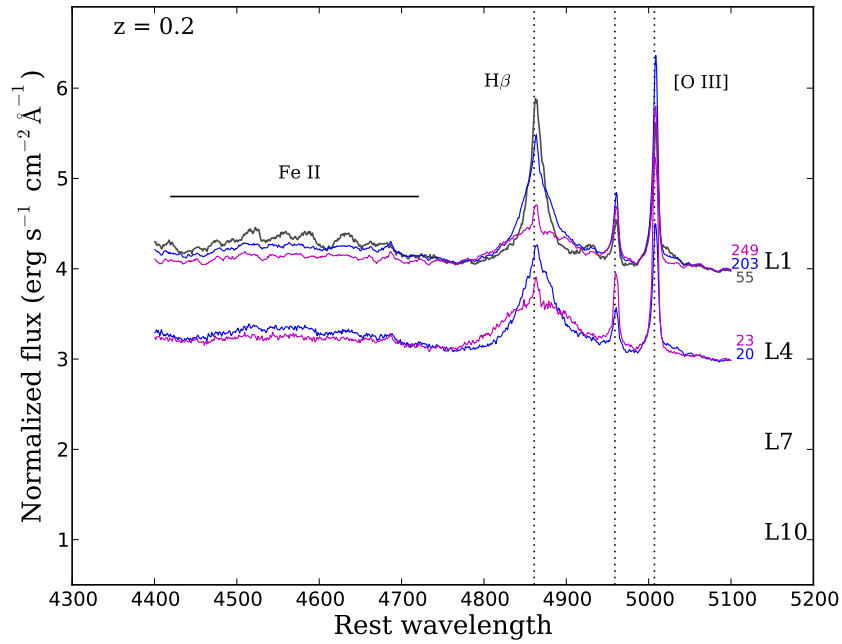


Figure A4. Same as Fig. A but for redshift bin centred at z= 0.2.

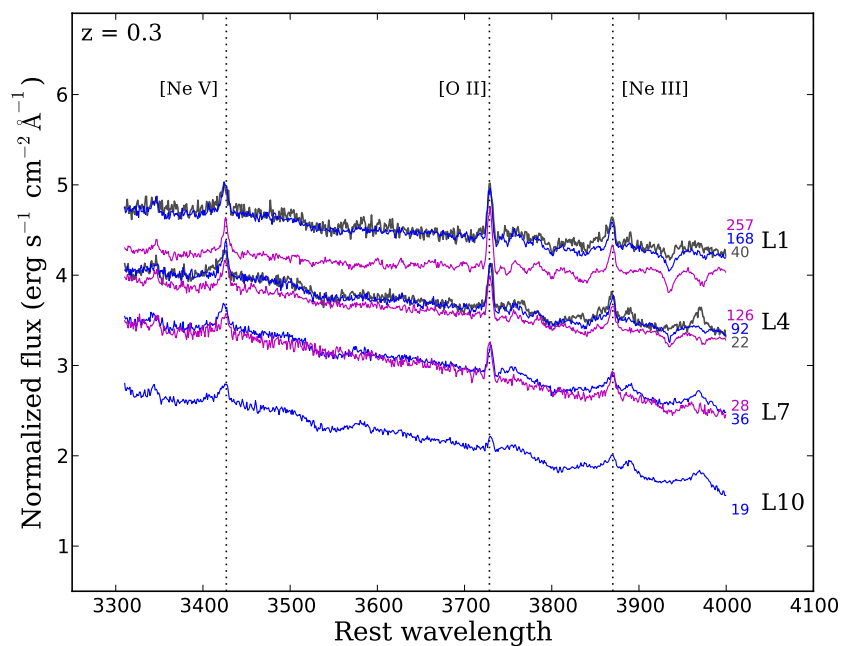


Figure A5. Same as Fig. A but for redshift bin centred at $z = 0.3$.

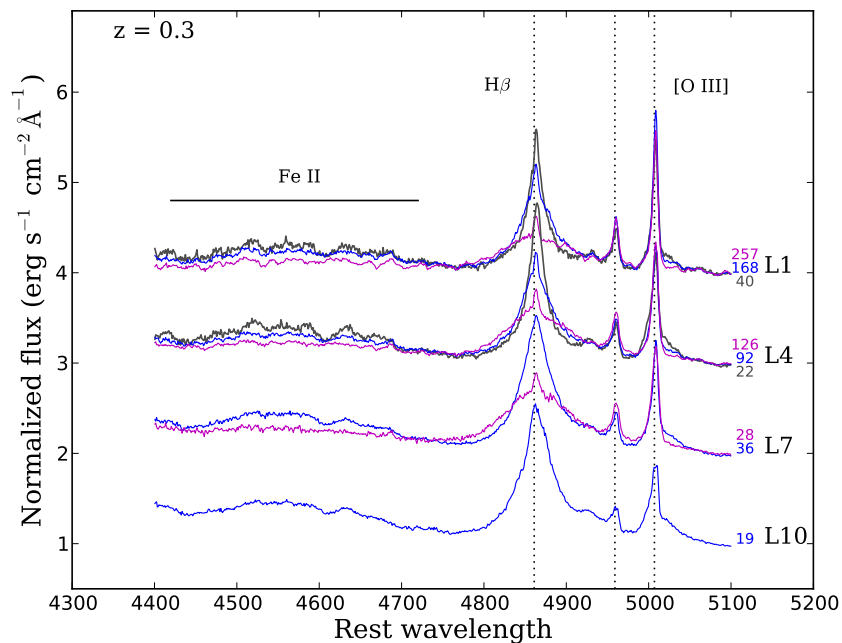


Figure A6. Same as Fig. A but for redshift bin centred at $z = 0.3$.

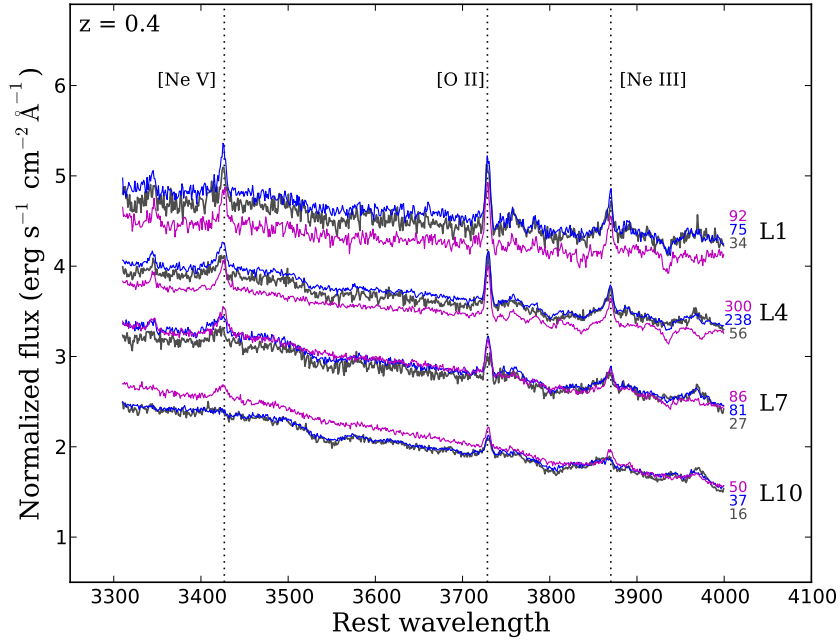


Figure A7. Same as Fig. A but for redshift bin centred at $z = 0.4$.

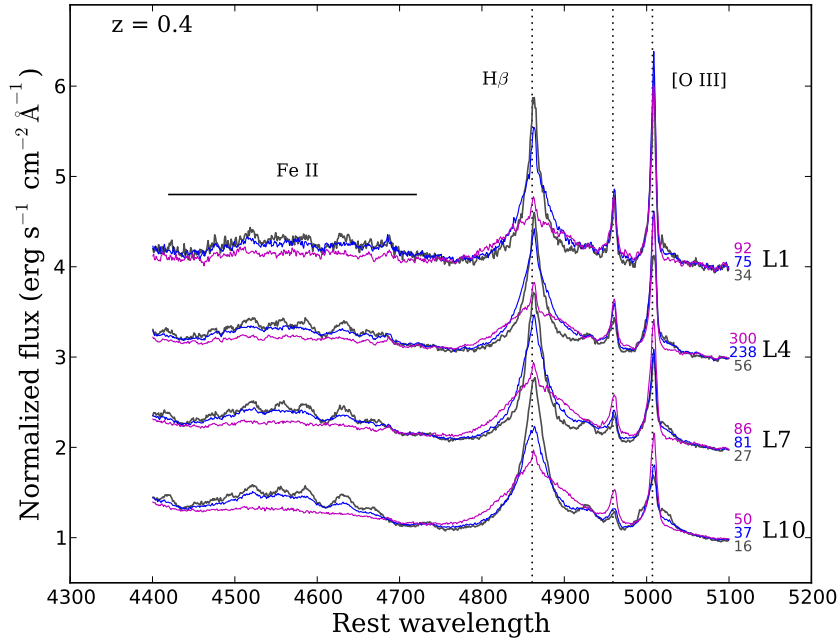


Figure A8. Same as Fig. A but for redshift bin centred at $z = 0.4$.

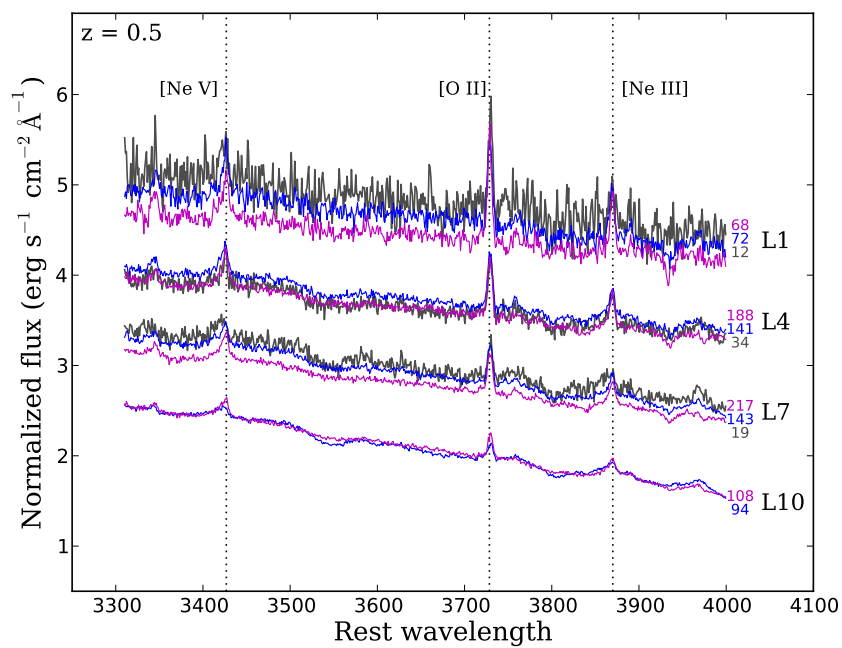


Figure A9. Same as Fig. A but for redshift bin centred at $z=0.5$.

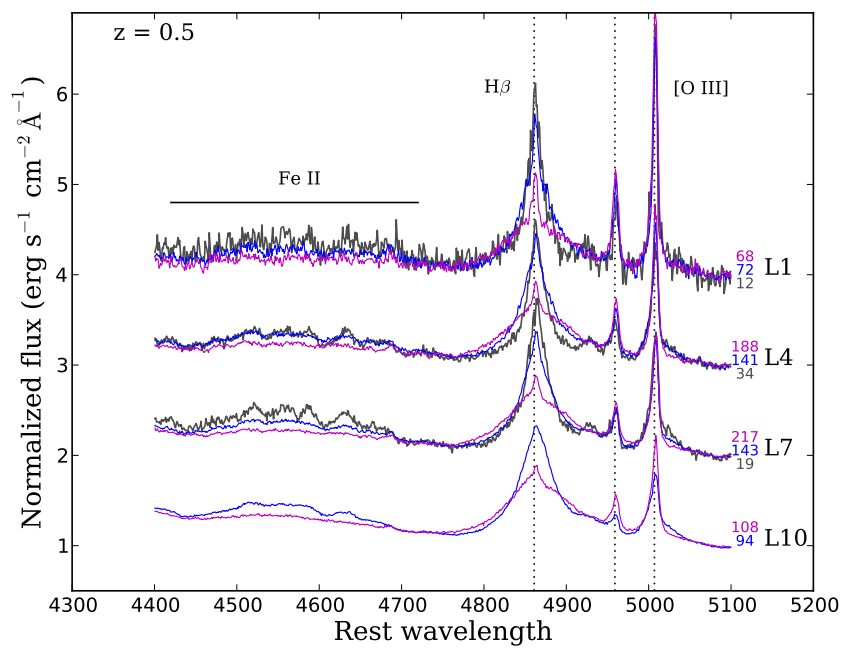


Figure A10. Same as Fig. A but for redshift bin centred at $z=0.5$.

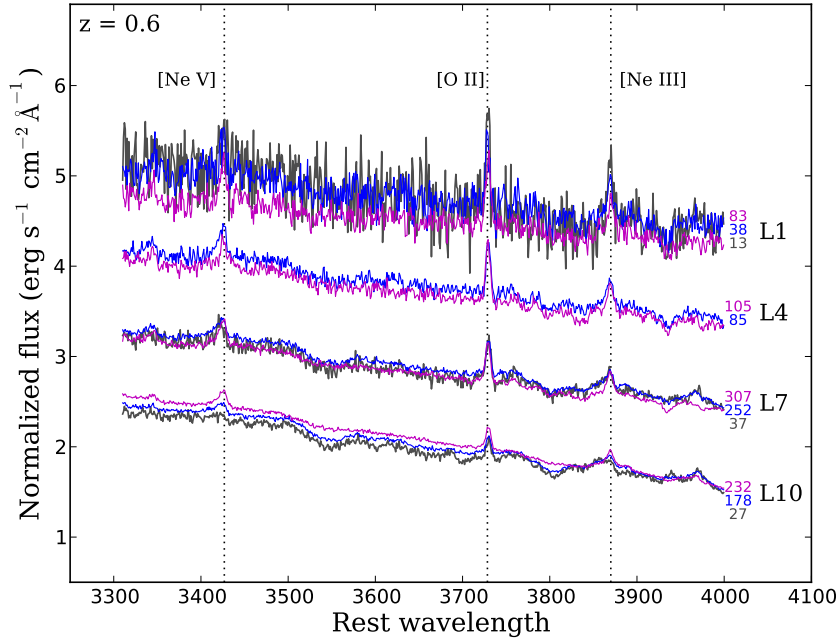


Figure A11. Same as Fig. A but for redshift bin centred at $z = 0.6$.

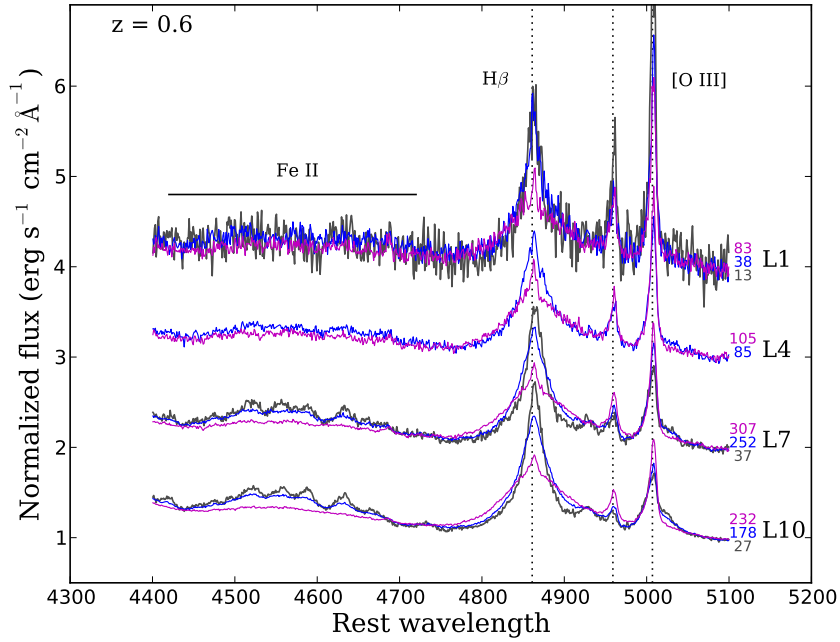


Figure A12. Same as Fig. A but for redshift bin centred at $z = 0.6$.

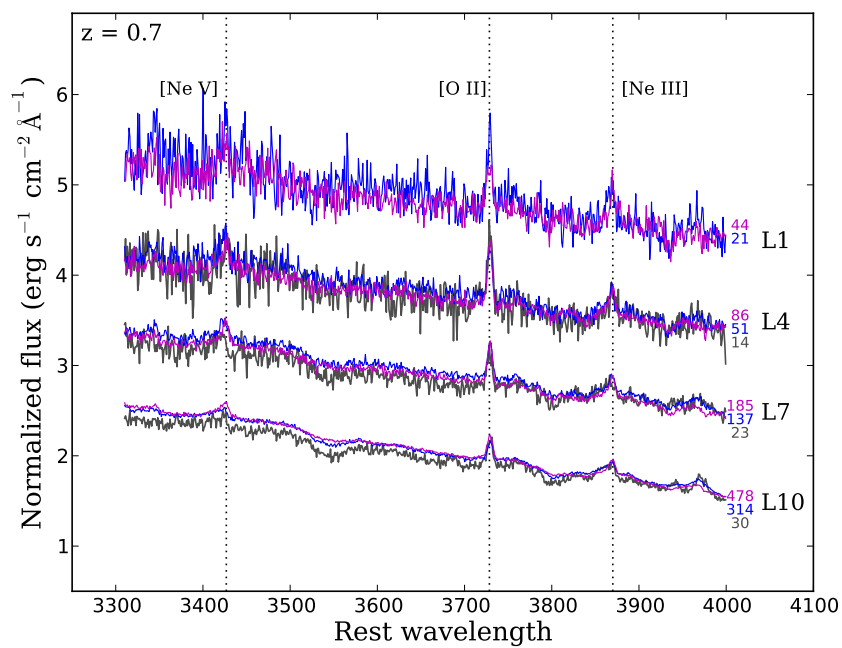


Figure A13. Same as Fig. A but for redshift bin centred at $z = 0.7$.

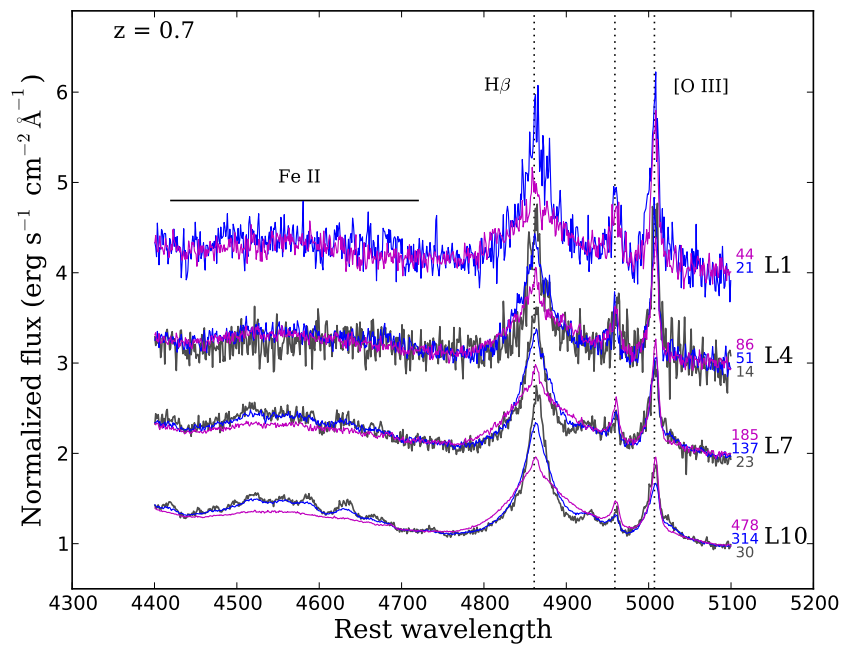


Figure A14. Same as Fig. A but for redshift bin centred at $z = 0.7$.